Supporting Information

A Magneto-responsive Nanomesh Biosensor for Simultaneous Mechanical Stimulation and Electrochemical Detection

This file includes:

Figs. S1 to S21

Legends for Movies S1 to S4

Supplementary Text

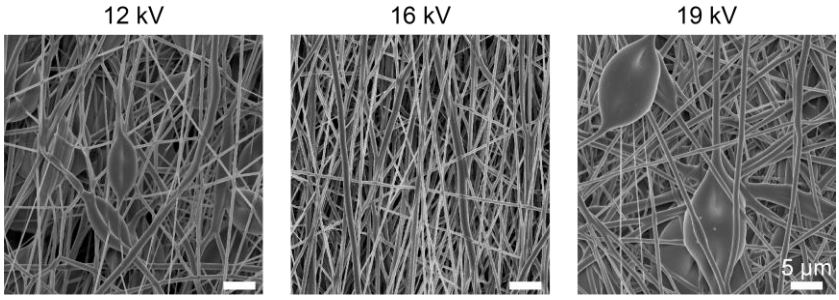

Fig. S1. SEM images of PU nanomeshes electrospun at different electrospinning voltage.

When the voltage is too low (12 kV) or too high (19 kV), it would lead to the formation of beaded fibers. The former is because the weak electric field force is difficult to counteract the surface tension of the droplet. The latter is due to the instability of the jet and the increased probability of polymer molecular chain breaking.

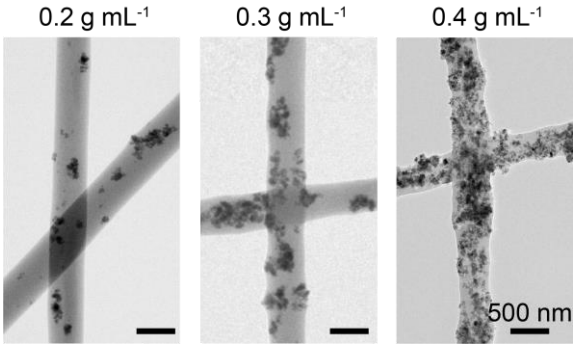

Fig. S2. TEM images of MRMs with different Fe_3O_4 NPs contents (0.2, 0.3, 0.4 and 0.5 g mL^{-1}).

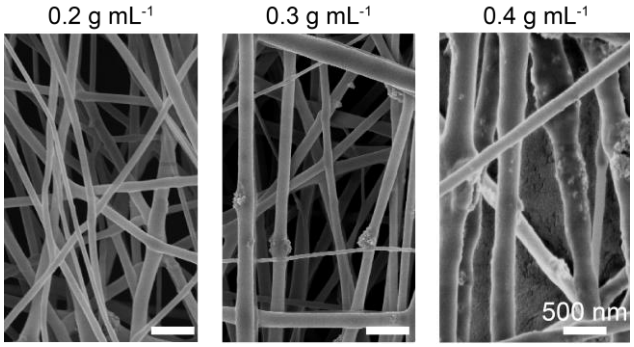

Fig. S3. SEM images of MRMs with different Fe_3O_4 NPs contents (0.2, 0.3, 0.4 and 0.5 g mL^{-1}).

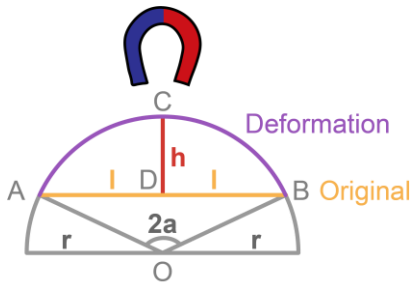

Fig. S4. Schematic diagram of approximate model for the MRM.

To quantify the deformation amplitude, the deformation of MRM was approximated as stretching from the chord (ADB) of the circle to the corresponding arc (ACB). Defining the length of chord ADB is 2l (L_{chord} = 2l), the height of arch CD is h (L_{arch} = h), the radius of the circle is r and the center angle of the circle corresponding to the chord ADB is 2a. The arc length (L_{arc}) could be calculated according to the intersection chord theorem.

According to the intersection chord theorem: $(2r - h)\,h = l^2$

$$r = (l^2 + h^2) / (2h)$$

$$\sin a = l / r = 2hl / (l^2 + h^2)$$

$$a = \arcsin[2hl / (l^2 + h^2)]$$

$$L_{arc} = a \times r = a \times (l^2 + h^2) / (2h)$$

For the experiment, L_{chord} is the length of MRM, so L_{chord} = 2l = 15 mm, the height of arch CD could be measured. For example, for MRM (Fe_3O_4 NPs content: 0.4 g mL^{-1}), the maximum value of arch height is 4 mm (L_{arch} = h = 4 mm), so L_{arc} = 17.7 mm.

And the deformation amplitude was defined as the ratio of increased chord length (L_{arc} - L_{chord}) to the original chord length (L_{chord}), that was (L_{arc} - L_{chord}) / L_{chord} × 100%.

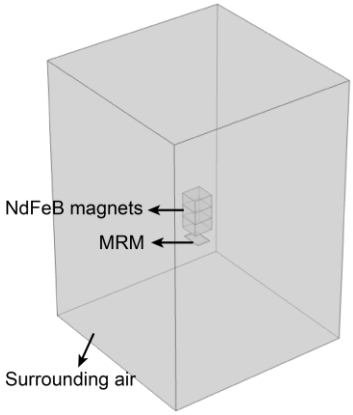

Fig. S5. Geometric structure of FEA model.

The FEA was conducted by COMSOL Multiphysics (COMSOL, Stockholm, Sweden) to predict how MRM deforms under magnetic fields. The geometric configuration of the model includes the bar-shaped magnet, MRM and surrounding air. We determined the dimensions of the magnet and nanomesh based on real-world conditions. The surrounding air domain was designed as a large rectangular prism measuring 140 mm $\times$ 140 mm $\times$ 200 mm to fully enclose the magnet and MRM.

Accurate material parameter input is crucial for precise computational results, particularly regarding the deformation of MRM. The primary parameters of interest include the density, Poisson's ratio, Young's modulus, and magnetic hysteresis loop parameters of the MRM. To ensure accurate input, we relied on experimental data for these parameters when configuring calculations in COMSOL. For MRM with varying Fe_3O_4 NPs content, it is worth noting that the density and Poisson's ratio of MRM remain constant at 1.49 $\times$ 10^3 kg m^{-3} and 0.3429, respectively, while Young's moduli and magnetic hysteresis loops vary among MRM with different Fe_3O_4 NPs content. Regarding material properties for air, accessible values can be obtained from the COMSOL material library under the "Air" category. For the magnetic material, a new material was created with a designated relative permeability (in this case, 4000), and its magnetic behavior was defined through the magnetization condition.

As for the configuration of boundary conditions and mechanical loading, a multiphysics coupling computation was designed, requiring the incorporation of both the Solid Mechanics and Magnetic Field (no current) nodes in COMSOL, each appropriately set up. The primary emphasis for boundary conditions is in the Solid Mechanics settings. We applied fixed constraints to the two shorter edges of the MRM to restrict its movement as in the real experimental scenario. Mechanical loading is achieved by magnetizing the magnet. In the Magnetic Field module, we opted for magnetic flux conservation, selected the magnet component, chose the magnetization mode, and

assigned a magnetization magnitude in the Z-direction. We could vary the magnetization intensity to impart magnetism to the magnet, thereby altering the magnet's magnetic strength.

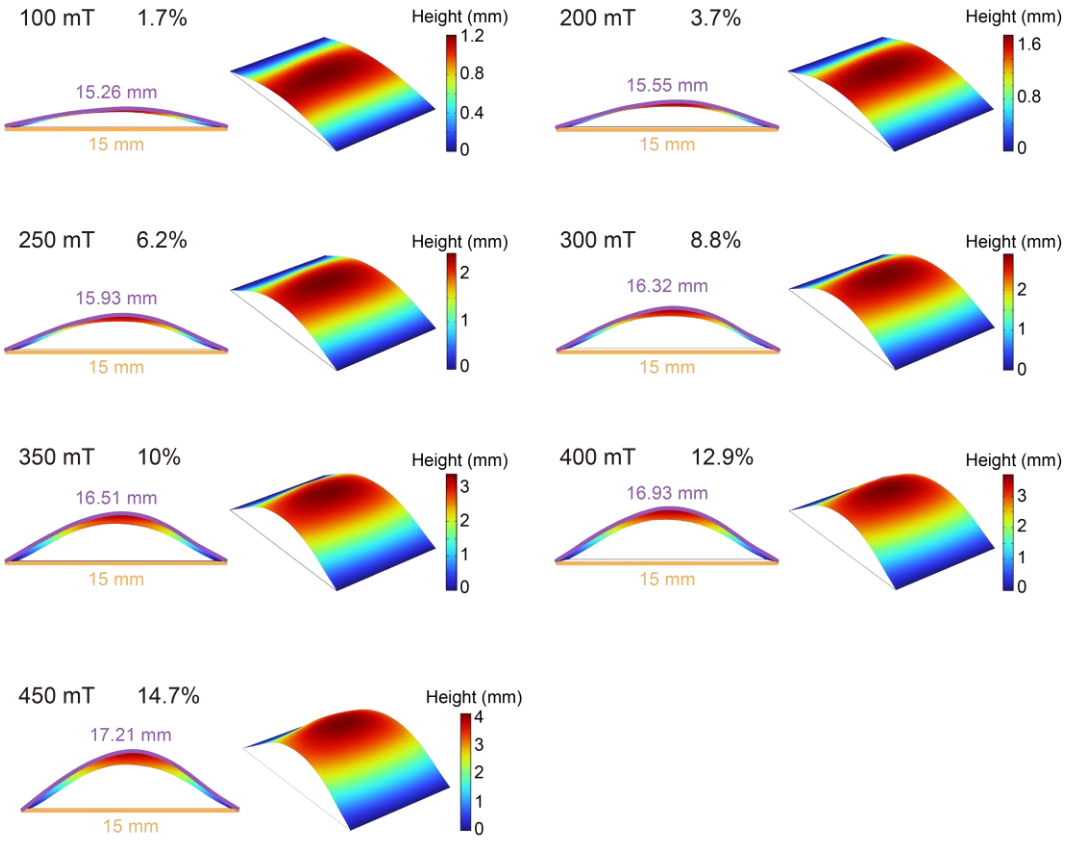

Fig. S6. Deformation diagrams of MRM calculated from FEA model under different magnetic induction intensity. The percentage values represent the deformation amplitude. Fe_3O_4 NPs content: 0.4 g mL^{-1}.

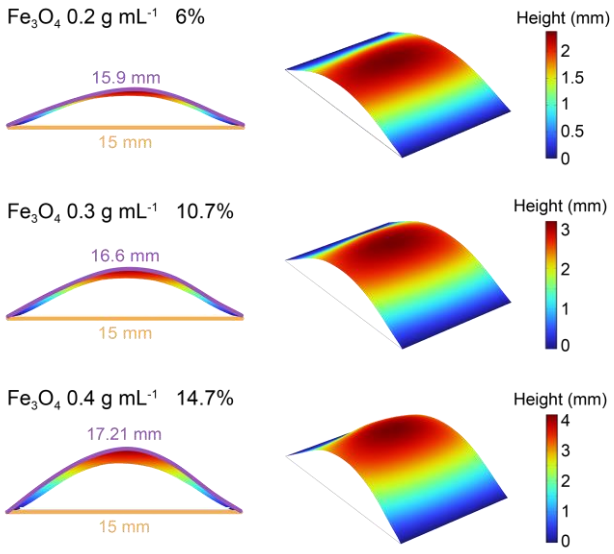

Fig. S7. Diagrams of maximum deformation of MRM with different Fe_3O_4 NPs content calculated from FEA model. The percentage values represent the deformation amplitude.

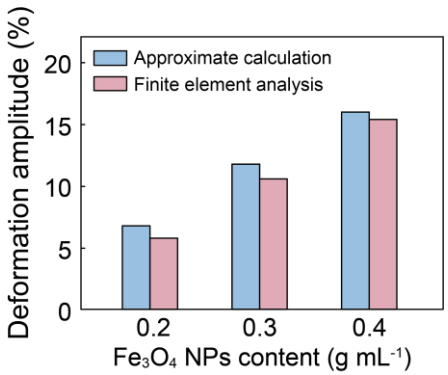

Fig. S8. Maximum deformation amplitude of MRM with different Fe_3O_4 NPs content calculated from approximate calculation and FEA.

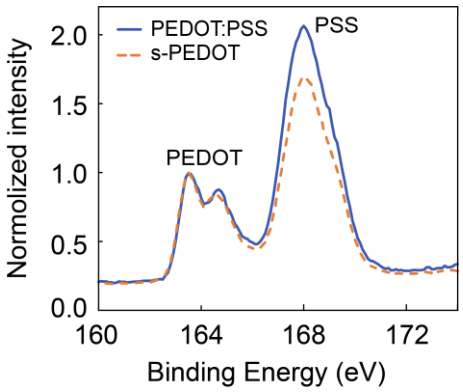

Fig. S9. S 2p XPS spectra of PEDOT and s-PEDOT.

The double peaks at binding energies of 163.5 eV and 164.7 eV corresponded to the S in PEDOT, while the peak around 168 eV corresponded to the S element in PSS. With the doping of D-sorbitol, the peak of PSS significantly decreased, which further proved the phase separation between PEDOT and PSS, and the separated PSS could be removed from the system through water washing.

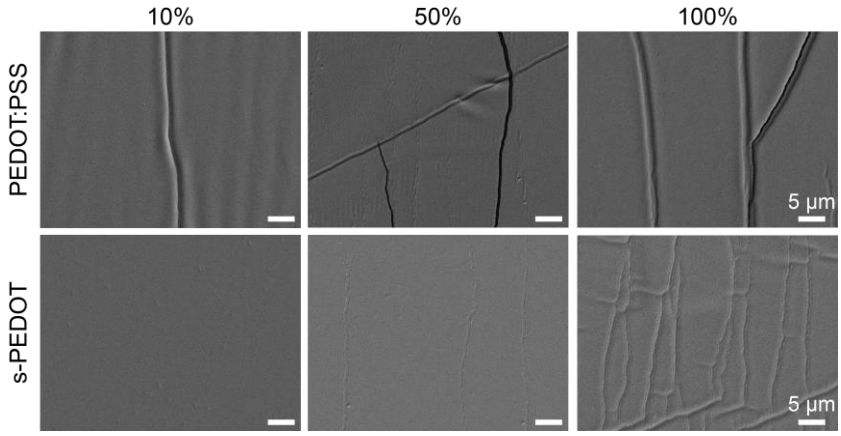

Fig. S10. SEM images of the PEDOT:PSS/PDMS and s-PEDOT/PDMS films after being stretched to various strains.

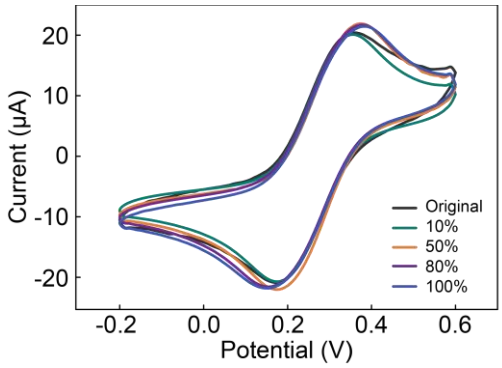

Fig. S11. CV curves of the s-PEDOT/PDMS electrode obtained in 1 mM $K_3[Fe(CN)_6]$ after being stretched to various strains. Scan rate: 50 mV s^{-1}.

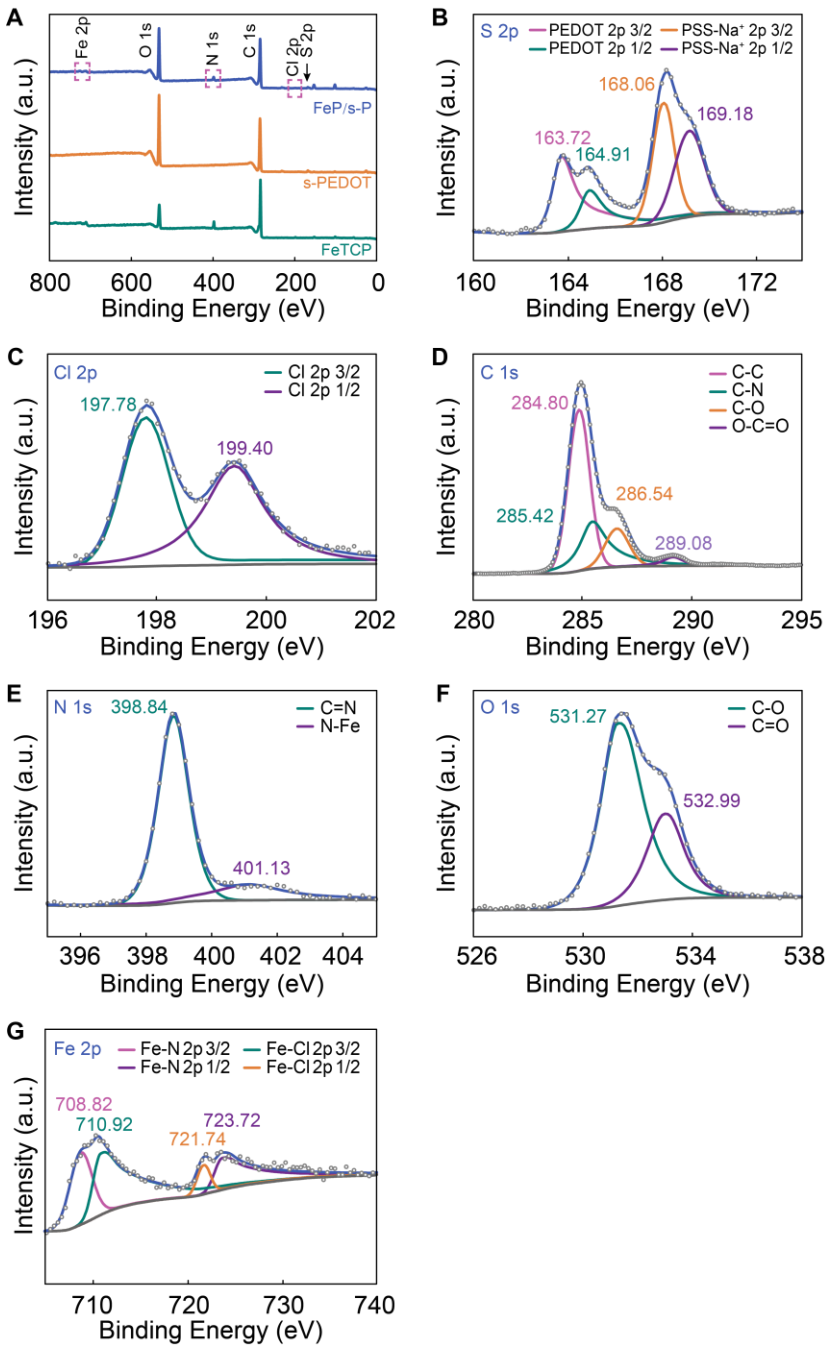

Fig. S12. (A) The full XPS spectra of FeP/s-P, s-PEDOT and FeTCP. XPS spectra of (B) S 2p states, (C) Cl 2p states, (D) C 1s states, (E) N 1s states, (F) O 1s states and (G) Fe 2p states of FeP/s-P.

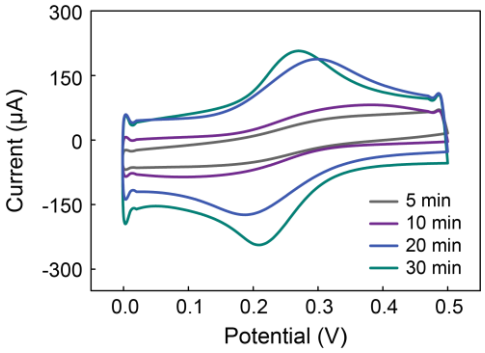

Fig. S13. CV curves of MRM@FeP/s-P sensors assembled in FeP/s-P solution for different time obtained in 1 mM $K_3[Fe(CN)_6]$. Scan rate: 50 mV s^{-1}.

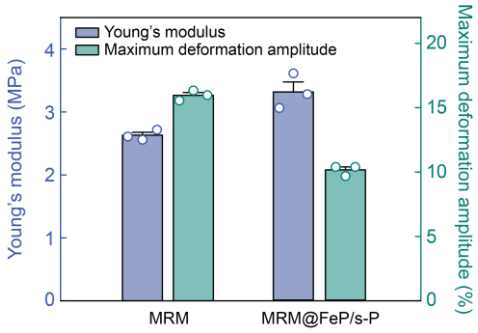

Fig. S14. Young's moduli and the maximum deformation amplitude of different MRMs. The data were presented as mean ± s.e.m. (n = 3, for each group); one-way ANOVA.

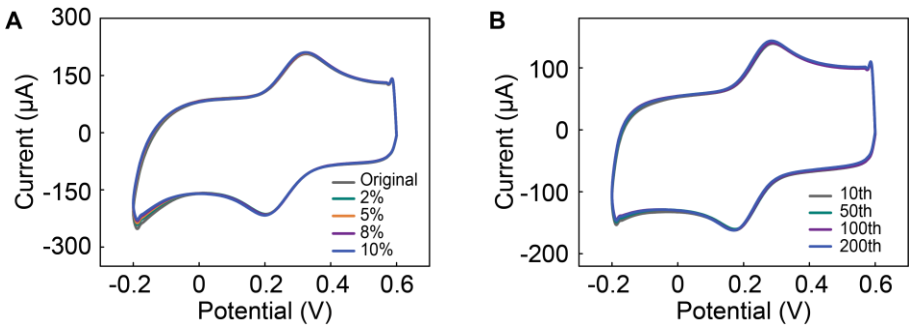

Fig. S15. CV curves obtained (A) after being stretched to various strains and (B) after being stretched to 10% for different times. Scan rate: 50 mV s^{-1}.

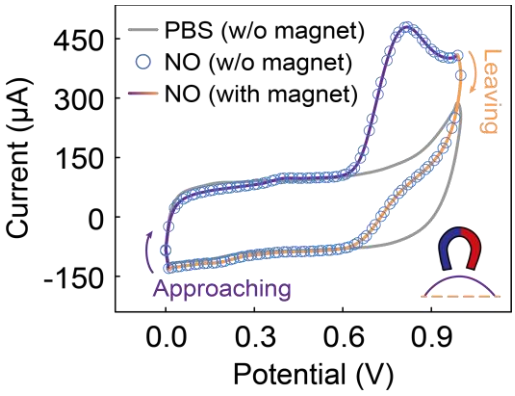

Fig. S16. CV curves of MRM@FeP/s-P sensor obtained in PBS with or without 50 μM NO during the magneto-responsive deformation process. Scan rate: 50 mV s^{-1}.

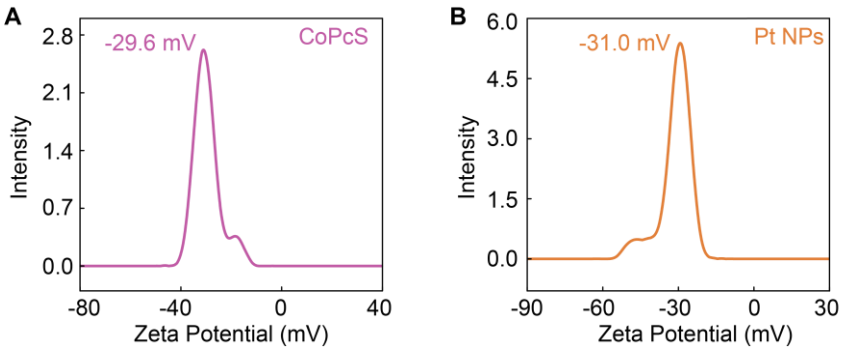

Fig. S17. Zeta potential of (A) CoPcS and (B) Pt NPs.

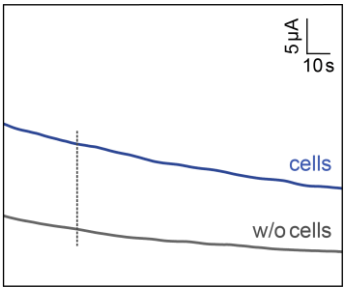

Fig. S18. Amperometric responses of MRM@FeP/s-P sensor immobilized on a glass slide to restrict its magneto-responsive deformation.

The MRM@FeP/s-P sensor was immobilized on the substrate to examine the influence of the magnetic field on electrochemical detection. The vertical gray line indicates the start of magnetic field application. Applied potential: +0.80 V vs. Ag/AgCl.

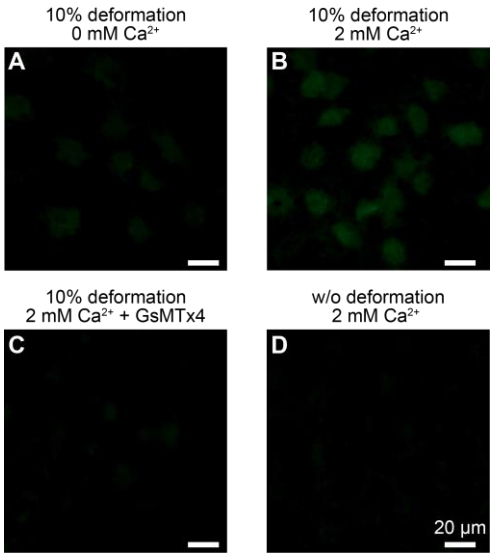

Fig. S19. Fluorescent images of intracellular Ca^{2+} under different conditions.

MC3T3-E1 cells in PBS with (**A**) 0 mM Ca^{2+}, (**B**) 2 mM Ca^{2+} and (**C**) 2 mM Ca^{2+} pretreatment with 10 μM GsMTx4 for 1 h exposed to 10% magneto-responsive deformation. (**D**) MC3T3-E1 cells in PBS with 2 mM Ca^{2+} without magnetic stimulation.

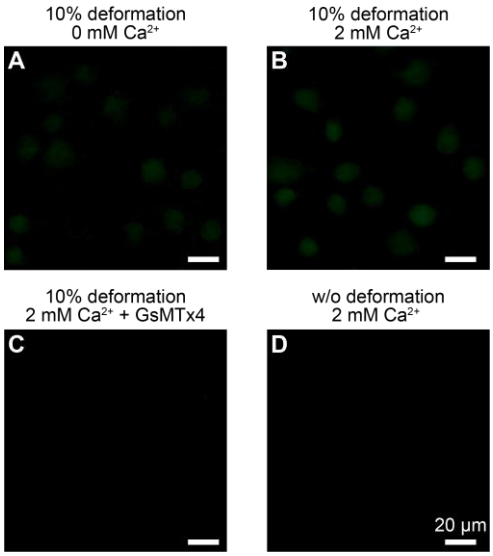

Fig. S20. Fluorescent images of intracellular NO under different conditions.

MC3T3-E1 cells in PBS with (**A**) 0 mM Ca^{2+}, (**B**) 2 mM Ca^{2+} and (**C**) 2 mM Ca^{2+} pretreatment with 10 μM GsMTx4 for 1 h exposed to 10% magneto-responsive deformation. (**D**) MC3T3-E1 cells in PBS with 2 mM Ca^{2+} without magnetic stimulation.

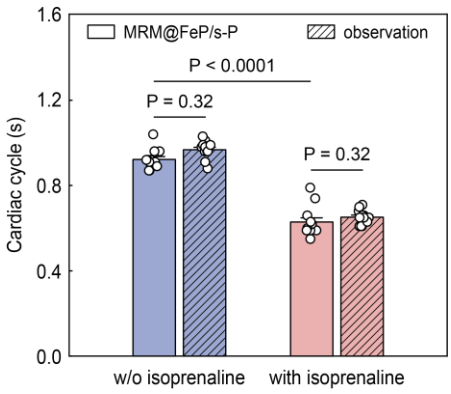

Fig. S21. Cardiac cycle time of the rat detected by the MRM@FeP/s-P sensor and observed before and after isoprenaline injection (n = 12, for each group). The data were presented as mean ±s.e.m.; one-way ANOVA.

Movie S1. Magneto-responsive deformation of MRM.

The deformation of MRM as the magnetic field approaches and recedes, capturing the dynamic response and movement of the nanomesh.

Movie S2. 3D magneto-responsive deformation of MRM.

The MRMs are patterned on both ends of two orthogonal rectangular PDMS elastic substrates. When exposed to an external magnetic field, the MRMs drive the substrates to deform into a three-dimensional structure.

Movie S3. Local magnetic manipulation of single nanofiber.

When the electromagnetic needle is energized, it generates a magnetic field that attracts the PU/Fe_3O_4 nanofiber.

Movie S4. Mechanical actuation of electrode and cells.

The rhodamine-labeled MRM@FeP/s-P sensor and CellTracker-labeled cells deform upward under the attraction of a magnetic field above, gradually moving away from the focal plane, causing the disappearance of red and green fluorescence in the movie.